

Improved Charge Transport and Reduced Non-Geminate Recombination in Organic Solar Cells by Adding Size-Selected Graphene Oxide Nanosheets

Joo-Hyun Kim,^{†,§} Dong Hun Sin,[†] Haena Kim,[†] Sae Byeok Jo,[†] Hansol Lee,[†] Joong Tark Han,^{*,‡} and Kilwon Cho^{*,†}

[†]Department of Chemical Engineering, Pohang University of Science and Technology, Pohang 37673, Korea

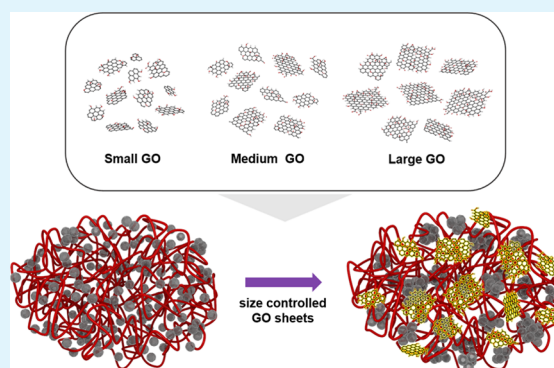
[‡]Nano Carbon Materials Research Group, Korea Electrotechnology Research Institute, Changwon 51543, Korea

[§]Clean Energy Research Center, Korea Institute of Science and Technology (KIST), Seoul 02792, Korea

S Supporting Information

ABSTRACT: Size-selected graphene oxide (GO) nanosheets were used to modify the bulk heterojunction (BHJ) morphology and electrical properties of organic photovoltaic (OPV) devices. The GO nanosheets were prepared with sizes ranging from several hundreds of nanometers to micrometers by using a physical sonication process and were then incorporated into PTB7:PC₇₁BM photoactive layers. Different GO sizes provide varied portions of the basal plane where aromatic sp²-hybridized regions are dominant and edges where oxygenated functional groups are located; thus, GO size distributions affect the GO dispersion stability and morphological aggregation of the BHJ layer. Electron delocalization by sp²-hybridization and the electron-withdrawing characteristics of functional groups p-dope the photoactive layer, giving rise to increasing carrier mobilities. Hole and electron mobilities are maximized at GO sizes of several hundreds of nanometers. Consequently, non-geminate recombination is significantly reduced by these facilitated hole and electron transports. The addition of GO nanosheets decreases the recombination order of non-geminate recombination and increases the generated carrier density. This reduction in the non-geminate recombination contributes to an increased power conversion efficiency of PTB7:PC₇₁BM OPV devices as high as 9.21%, particularly, by increasing the fill factor to 70.5% in normal devices and 69.4% in inverted devices.

KEYWORDS: graphene oxide nanosheet, graphene oxide size, bulk heterojunction, organic solar cell, p-dope, carrier mobility, charge transport, non-geminate recombination



1. INTRODUCTION

Organic photovoltaic (OPV) devices have potential applications as clean energy sources and flexible solution-processed electronic devices.¹ Their power conversion efficiencies (PCEs) have been increased to >10% by using newly synthesized conjugated polymers.^{2–4} This achievement has been accelerated over the recent years from the emergence of small molecular acceptors^{5–12} that demonstrate outstanding optical and electrical properties, and the record efficiency reaches over 14%.¹² However, the limited exciton diffusion length and charge carrier mobility of organic solar cells (OSCs) restrict their PCEs to less than those of their inorganic counterparts. To reduce this difference, bulk heterojunction (BHJ) morphology control^{13–23} and ternary blend systems^{24–27} that contain embedded nanoparticles (NPs)^{28,29} have been investigated in attempt to increase the PCEs of OPV devices.

Silver (Ag) and gold (Au) NPs have been added into BHJ active layers to induce localized surface plasmon resonance (LSPR), which can couple with incident light. This light is scattered and reflected by the metallic NPs in the dielectric environment; this phenomenon increases the number of optical paths within the BHJ active layer and thus increases the optical absorption.^{30–33} Inorganic nanomaterials with different shapes such as nanocrystals, nanorods, and quantum dots have been dispersed in the photoactive layers as electron acceptors.^{34–36} Those inorganic NPs are also applied to improve the electrical properties of charge transport and charge selectivity.^{37–40} Although metal NPs have shown various functions in OPV devices, the use of metal NPs has shown limited contributions to the photovoltaic character-

Received: December 18, 2018

Accepted: May 10, 2019

Published: May 10, 2019

tics;^{28–40} the conversion of absorbed photons into photocurrent has not to date been significantly increased, and the presence of metal NPs in BHJ photoactive layers frequently degrades the carrier transport when the ternary morphology cannot be properly controlled. Also, inorganic nanomaterials are not reproducible in processing, which requires elaborate and expensive experimental procedures to produce consistent optoelectronic properties.

Incorporating graphene oxides (GOs) into the BHJ active layer improves the photovoltaic efficiencies of OPV devices by tuning their optoelectronic properties.^{41–50} The band gap structures of reduced GO nanosheets (NSs) can be modulated by varying their level of doping,⁴⁹ and the conductivity of graphene quantum dots is increased by tuning the degree of reduction.⁵⁰ Two-dimensional GO NSs contain sp²-hybridized carbon region as well as disordered area with oxygenated functional groups on their basal planes and at the edges; these characteristics cause variations of electrical properties.^{41–51} However, the use of GO NSs necessitates the use of complicated chemical treatments; furthermore, those optoelectronic properties produced by adding GO NSs have been neither completely quantified nor properly tuned to maximize the efficiencies of the OPV devices.

In this study, we added size-selected GO NSs^{52,53} to BHJ photoactive layers that consist of BDT-thieno[3,4-b]thiophene (PTB7) and [6,6]-phenyl-C71-butyric acid methyl ester (PC₇₁BM). The GO NSs were prepared with sizes ranging from hundreds of nanometers to several micrometers by using a physical sonication process without any chemical treatments of reduction or oxidation and then just dispersed in *N*-methyl-2-pyrrolidone (NMP). The influences of oxygenated electron-withdrawing functional groups of GO NSs on morphology variations and p-doping characteristics^{41–48} of OPV devices were inspected by image analyses and evaluation of the electrical characteristics of space-charge-limited current (SCLC) devices and field-effect transistors (FETs). Incorporation of GO NSs into the photoactive layer greatly reduces the non-geminate recombination of charge carriers, which was estimated from the carrier lifetime, carrier density, and recombination reaction order by performing transient photovoltage/transient photocurrent (TPV/TPC) measurements.^{54–56} The reduced non-geminate recombination of photovoltaic devices that incorporate the GO NSs increases the photocurrent and fill factor (*FF*) to 70.5% in normal devices and 69.4% in inverted devices. The size-selected GO NSs formed by the physical sonication process tune the charge transport and recombination properties and thereby significantly increase the efficiency of PTB7:PC₇₁BM OPV devices as high as 9.21% in the inverted structure.

2. EXPERIMENTAL SECTION

2.1. Fabrication and Characterization of the GO NSs. GO NSs were prepared by oxidizing and exfoliating graphite powder (Alfa Aesar, 99.999% purity, –200 mesh) using a modified Hummers method (Supporting Information).^{45,57} Graphite oxide powder samples were exfoliated to produce GO NSs by horn sonication of 1 g/L solutions for specified periods. The GO NSs were sorted by centrifugation at 10,000 rpm for 1 h, and the supernatant solution was then decanted. Each sediment was redispersed in water to the same volume, and the centrifugation and decanting steps were repeated to prepare the size-selected GO NSs.

2.2. Device Fabrication and Electrical Characterization.
2.2.1. Device Fabrication. ITO substrates were cleaned sequentially with detergent, distilled water, acetone, and isopropyl alcohol. The

ZnO precursor solution was prepared by mixing zinc acetate dihydrate [Zn(CH₃COO)₂·2H₂O] and ethanolamine in 2-methoxyethanol. The ZnO film was fabricated by spin-casting the ZnO precursor solution onto ITO substrates, which was subsequently annealed in air at 150 °C. The PTB7:PC₇₁BM blend solution was prepared at 40 °C for 24 h. Each GO NS sample was added to the solution, and diiodooctane (DIO; 3% by volume) was also added just before casting. Photoactive layers (100 nm thickness) were deposited by spin-casting the blend solutions onto ZnO-coated ITO substrates. MoO₃/Al electrodes were deposited by using thermal evaporation under a high vacuum (1 × 10^{–6} mbar) to fabricate inverted devices. We also used the structure of ITO/PEDOT:PSS/BHJ layer/Ca/Al for normal devices. Hole mobilities (μ_h) and electron mobilities (μ_e) were evaluated by fabricating hole-only and electron-only devices with PEDOT:PSS/Pd and Al/Al as the anodes and cathodes, respectively. FETs with top-contact structures were fabricated to have gate electrodes composed of heavily doped n-type Si wafers, gate dielectric of thermally oxidized SiO₂ layer (300 nm), and Ti/Au electrodes.

2.2.2. Electrical Characterizations. The current density–voltage (*J–V*) characteristics were recorded using a source measurement unit (Keithley 4200) under AM 1.5G solar illumination with an intensity of 100 mW cm^{–2} (Oriel 1 kW solar simulator). The light intensities were calibrated with respect to a reference silicon solar cell (PVM 132) guaranteed by the National Renewable Energy Laboratory (NREL). The incident photon-to-current conversion efficiencies (IPCEs) were measured using a photomodulation spectroscopy set-up (Merlin, Oriel) with monochromatic light from a xenon lamp. The SCLC carrier mobilities were evaluated using the Mott–Gurney square law from eq 1^{58,59}

$$J = \frac{9}{8} \epsilon_0 \epsilon_r \mu \frac{V^2}{L^3} \quad (1)$$

where $\epsilon_0 \epsilon_r$ is the permittivity of the polymer, and μ is the charge carrier mobility.

The FET carrier mobilities were measured in a vacuum condition (Keithley 2400) and evaluated using eq 2^{21,41}

$$\mu = \frac{Lg_m}{WC_0V_{ds}} \quad (2)$$

where *W* is the channel width, *L* is the channel length, $g_m = dI_{ds}/dV_{gs}$ is the transconductance, *C*₀ is the capacitance, and *V*_{ds} is the drain–source voltage.

2.2.3. TPV/TPC Measurements. From the TPV and TPC measurements, we could estimate the carrier lifetime ($\tau_{\Delta n}$) and charge carrier density (*n*), respectively. For TPV measurements, the devices were connected directly to an oscilloscope under open-circuit conditions (1 MΩ) and illuminated under a white light LED at a range of illumination levels. A small optical perturbation by a laser diode was used to produce a voltage perturbation. The TPCs were measured under short-circuit conditions at a steady state with a short-lived perturbation at various light intensities. The number of charges generated by each pulse was evaluated by integrating a photocurrent (50 Ω) without the bias light. The recombination exponent (λ) was estimated from a regression of $\tau_{\Delta n}$ on *n* by eq 3, and then reaction order *R* is obtained by $R = \lambda + 1$ ^{54–56}

$$\tau_{\Delta n} = \tau_{\Delta n_0} \left(\frac{n_0}{n} \right)^\lambda \quad (3)$$

where $\tau_{\Delta n_0}$ and *n*₀ are the constants.

2.2.4. Optical and Morphological Characterizations. Light absorption of the photoactive layer was estimated by measuring the reflectance spectra using a UV–vis spectrophotometer (Cary 5000, Varian) with an integrating sphere. The emission spectrum was measured using a spectrofluorometer (FP-6500, Jasco). The morphologies of the blend films were characterized using a transmission electron microscope (TEM, Hitachi 7600) and an atomic force microscope (Bruker, NanoScope V) operated in tapping mode with a silicon cantilever.

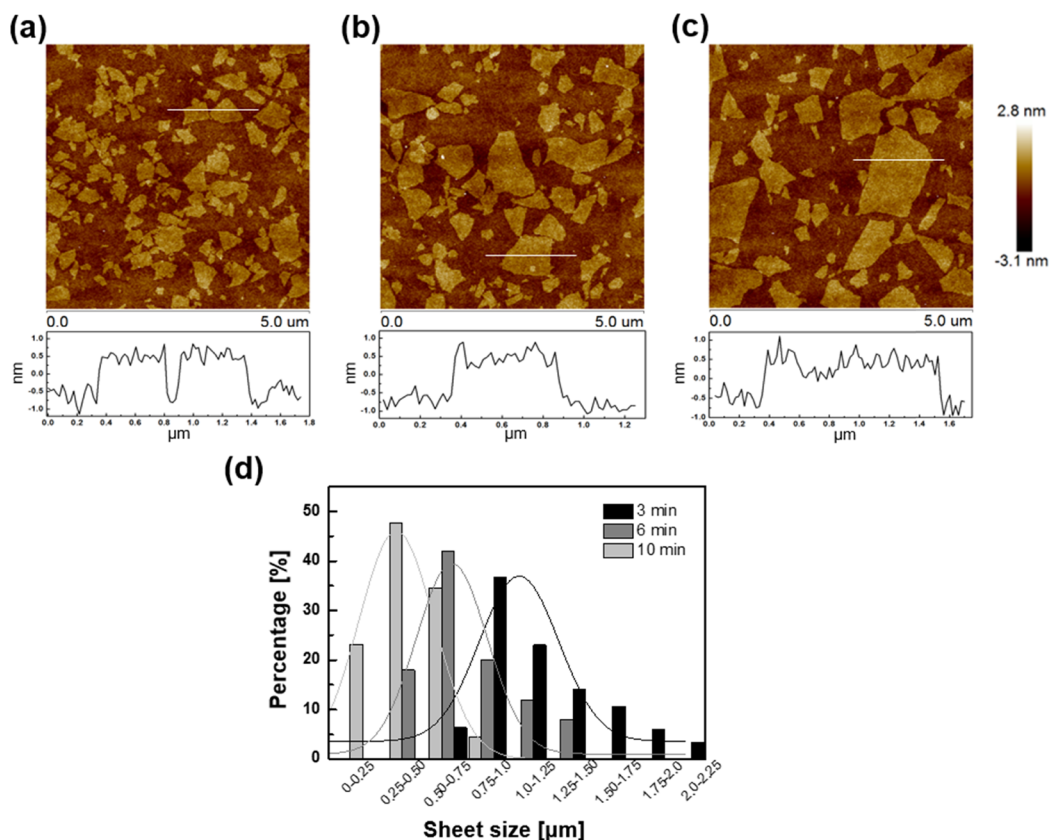


Figure 1. AFM height images and height profiles of GO NSs with different sizes: (a) SGO, (b) MGO, and (c) LGO NSs. (d) Their size distributions obtained using different sonication times.

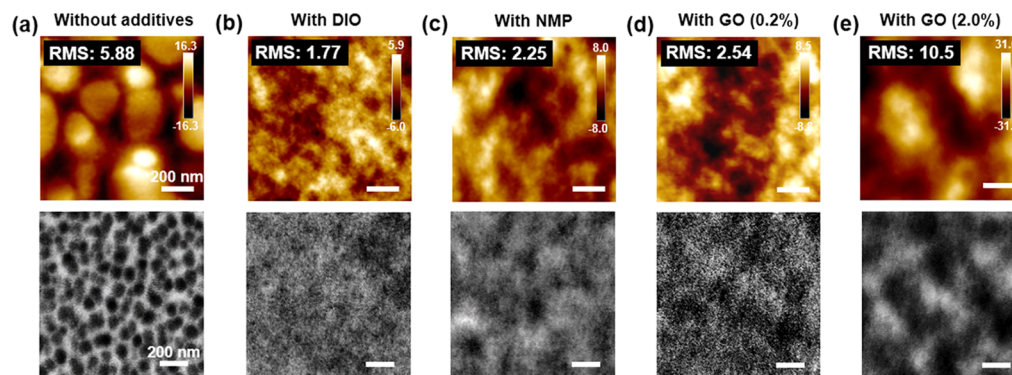


Figure 2. AFM height images (top) with RMS roughness and TEM images (bottom) of PTB7:PC₇₁BM blend films: (a) without additives, (b) with DIO, (c) with NMP, (d) with MGO (0.2 wt %), and (e) with MGO (2.0 wt %).

3. RESULTS AND DISCUSSION

GO NSs contain the aromatic region with sp^2 -hybridized carbon and oxygenated region with electron-withdrawing functional groups.^{45,51–53} Aromatic carbons and the functional groups such as hydroxyl, epoxy, and carbonyl groups are mainly placed on the basal plane of GO NSs, whereas ionizable carboxylic functional groups are mostly located at the edges.^{45,51–53} The characteristics of the GO NSs, such as carbon double bonds and carbonyl functional groups, were confirmed using XPS, C13-NMR, and FT-IR (Figure S1). Raman spectra of GO NSs show both D and G bands at ~ 1330 and ~ 1600 cm^{-1} , respectively, with a D/G ratio of 1.43. This result confirms the quality of GO NSs when they are compared to the previous measurements (Figure S2).⁶⁰ The

dispersion medium was changed from water to NMP to ensure good mixing of the GO NSs in the photoactive layer. NS samples of small GO (SGO), medium GO (MGO), and large-sized GO (LGO) (Figure 1a–c and Figure S3) were obtained using sonication times of 10, 6, and 3 min, respectively. Each GO NS sample was incorporated into a photoactive layer with PTB7 and PC₇₁BM. The nanomorphologies and device properties affected by the DIO additive⁶¹ and size of GO NSs will be discussed in the following section.

3.1. BHJ Morphology Variations by Adding Size-Selected GO NSs. Size selection yields GOs with three size ranges: SGO is mainly 250 to 500 nm, MGO is mainly 500 to 750 nm, and LGO is micrometers in size (Figure 1a–c and Figure S3), with a few above and below those ranges in all groups (Figure 1d). AFM height profiles confirm these sizes,

and that the GO NSs are ~ 1 nm-thick (Figure 1). The sample of each GO NS was incorporated into BHJ photoactive layers (Figure 2). The addition of DIO yields a uniform morphology without large phase segregation (Figure 2b).⁶¹ However, when the MGO NS (0.2 wt %) in the NMP solvent is added to the BHJ layer, the GO NSs induce formation of aggregated morphologies (Figure 2d). When 2.0 wt % GO NSs in NMP is added to the blend film, the PTB7:PC₇₁BM photoactive layer is severely phase-separated with a high root-mean-squared (rms) roughness (Figure 2e).

The sizes of the NSs affect the morphologies of the BHJ layer. The RMS roughness is higher for the active layer with LGO than for the layers with SGO and MGO (Figure S4). LGO has a smaller edge portion for a given area where carboxylic functional groups exist than SGO and MGO do.^{52,53} Fewer defect sites occur in the basal plane in LGO where oxidation might occur than in SGO and MGO; the number of defect sites in LGO might be decreased by reducing the sonication time during processing.^{52,53} These oxygenated carboxylic functional groups induce repulsive interaction among GO NSs and thereby contribute to GO dispersion stability.^{52,53} In LGO, the repulsive interactions are reduced due to the decreasing carboxylic functional groups and increased carbon region; as a result, attraction among GO sheets increases and LGO dispersion stability decreases. Therefore, reduced LGO dispersion stability yields aggregation between GO layers themselves and between the BHJ morphology and GO layers. The high concentration of GO NSs also provides the strong attraction among GO NSs, so the BHJ morphology becomes aggregated (Figure 2e). In the grazing incidence X-ray diffraction (GIXRD) results, the nanoscale crystalline structures of PTB7 evaluated by a (100) lamellar peak in the out-of-plane (OOP) direction, and the amorphous PC₇₁BM characteristics near $1.35 q$ do not vary significantly by adding GO NSs (Figure S5); this lack of GO NS effect indicates that the aggregation in the blend morphology does not change the molecular ordering of constituent components.^{62,63}

3.2. Charge Carrier Mobilities of Devices with Size-Selected GO NSs. SCLC measurements were performed to estimate the charge carrier mobilities of devices with GO NSs of three sizes at various concentrations. The hole and electron mobilities (Figure 3 and Table S1) were extracted from the J_D curves of the hole-only and electron-only devices (Figure S6), respectively.^{58,59} Addition of 0.2 wt % MGO increases μ_h to $4.15 \times 10^{-4} \text{ cm}^2 \text{ V}^{-1} \text{ s}^{-1}$ and μ_e to $8.26 \times 10^{-4} \text{ cm}^2 \text{ V}^{-1} \text{ s}^{-1}$.

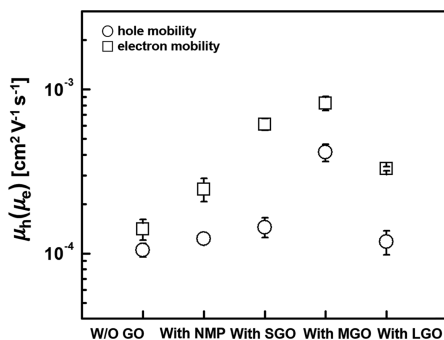


Figure 3. Hole (○) and electron mobilities (□) measured from SCLC devices in hole-only and electron-only device configurations, respectively.

These values are higher than in devices without GO NSs (with DIO): $\mu_h = 1.05 \times 10^{-4} \text{ cm}^2 \text{ V}^{-1} \text{ s}^{-1}$; $\mu_e = 1.41 \times 10^{-4} \text{ cm}^2 \text{ V}^{-1} \text{ s}^{-1}$. Addition of NMP to the photoactive layer also leads to a higher μ_h of $1.23 \times 10^{-4} \text{ cm}^2 \text{ V}^{-1} \text{ s}^{-1}$ and a μ_e of $2.47 \times 10^{-4} \text{ cm}^2 \text{ V}^{-1} \text{ s}^{-1}$ than the μ_h and μ_e of the photoactive layer fabricated only with DIO but has lower μ_h and μ_e than in the MGO devices. However, the addition of LGO to the photoactive layer reduces μ_h and μ_e compared to the values from MGO devices.

To corroborate the SCLC mobilities, we fabricated FETs and evaluated the FET carrier mobilities from curves of drain current on gate voltage (Figure 4a).^{21,41} Addition of 0.2 wt % SGO, MGO, and LGO increases μ_h from 8.33×10^{-4} to 2.06×10^{-3} , 2.02×10^{-3} , and $3.83 \times 10^{-3} \text{ cm}^2 \text{ V}^{-1} \text{ s}^{-1}$, respectively, and causes shifts in the threshold voltage (V_{th}) from -32.7 to -29.9 , -3.95 , and -7.88 V , respectively (Figure 4b). P-type

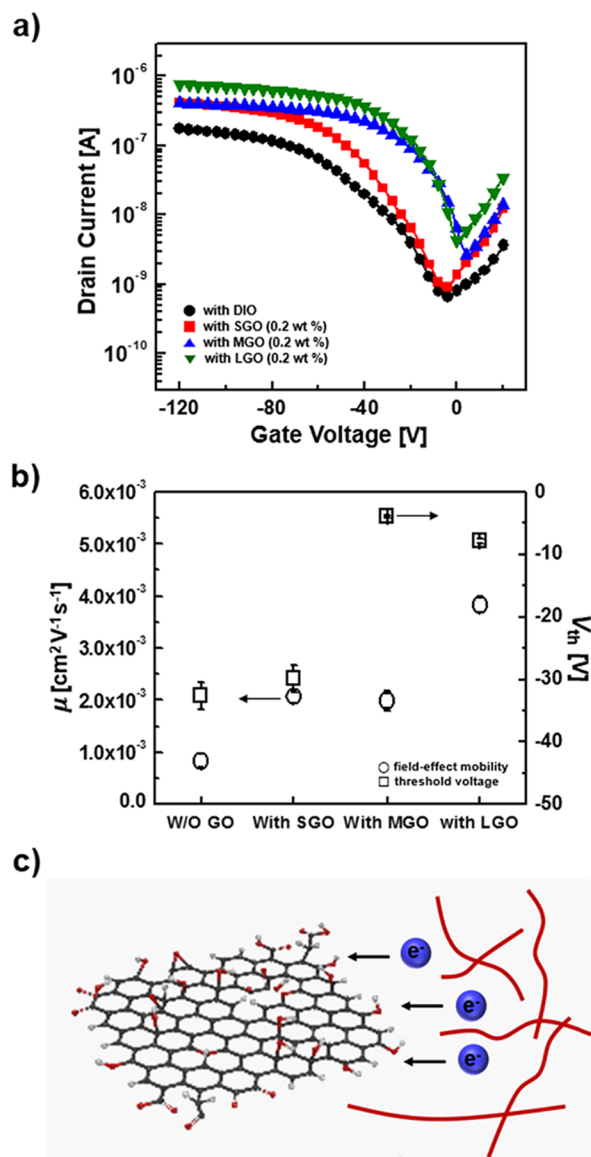


Figure 4. (a) Transfer characteristics of top contact PTB7:PC₇₁BM transistors with Au electrodes. The P-mode was measured by applying negative gate voltages with a drain electrode biased at -40 V . (b) FET mobilities and threshold voltages obtained from FET with SGO, MGO, LGO, and without GO NSs. (c) Scheme of p-doping of the photoactive layer by GO NSs.

doping of the photoactive layer by the GO NSs is evident in the transfer curve of top-gate FET, which shows increasing μ_h and positive shifts in V_{th} , as is typical of p-doping (Figure 4b).^{41,48} The increase in the carrier mobility is a result of p-doping induced by electron-withdrawing functional groups.^{41–48} These functional groups dissociate to produce protons, which extract electrons and p-dope the PTB7, working as a hole transport layer (Figure 4c).^{41–48} The FET carrier mobility and p-doping increase with increasing GO size. This is considered to be related to the increasing aromatic region with sp^2 -hybridization and decrease in the number of defect sites, because these changes facilitate electron delocalization, stabilize negative charges, and thus increase both electron and associated hole mobilities.^{51–53} LGO facilitates hole transport in lateral direction, which is measured by FET devices but not in the vertical direction, which is evaluated by the SCLC devices because GO aggregation and lateral two-dimensional geometry of GO NSs hamper charge transport in the vertical direction.⁴⁸

3.3. Photovoltaic Properties of OPV Devices Containing Size-Selected GO NSs. Solar cells were fabricated to determine the influence of the GO NSs on their electrical properties. SGO, MGO, and LGO samples were each added into a PTB7:PC₇₁BM BHJ photoactive layer in normal (Figure S7, S8, Table S1, and S2) and inverted devices (Figure 5 and

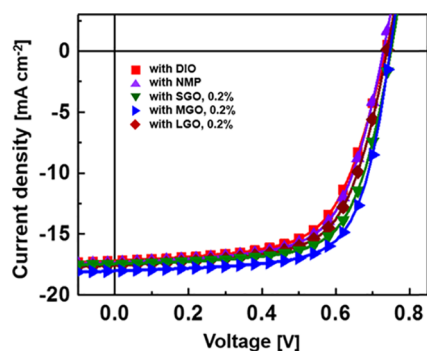


Figure 5. Current density–voltage (J – V) curves of the PTB7:PC₇₁BM inverted devices based on photoactive layers prepared with various sized GO NSs, DIO, and NMP measured under illumination at 100 mW cm⁻² (simulated AM 1.5G).

Table 1). Various GO NS concentrations (0.1, 0.2, 0.4, 1.0, and 2.0 wt %) were included to the BHJ layers with the aim of optimizing the PTB7:PC₇₁BM normal device (Figure S8). Various sized GO NSs were also incorporated into P3HT:PC₇₁BM layers to verify the effect of GO NSs (Figure S9). The photovoltaic properties of devices with GO NSs were

compared to those of devices with NMP to distinguish the effects of the GO NSs from those of the NMP solvent. The effects of the variations in size distributions and GO concentrations on the photovoltaic parameters were evaluated, and these results are summarized in Table 1 and Table S1.

Photovoltaic properties of PTB7:PC₇₁BM devices are optimized at 0.2 wt % MGO. At this condition, the PCE of the PTB7:PC₇₁BM inverted device increases to 9.09% (highest PCE is 9.21%) due to increases in the photocurrent generation and FF as high as 69.4%, whereas the device with only DIO has a PCE of 7.94% (Table 1). The increases in short-circuit current density (J_{sc}) and FF are caused by the reduced series resistance (R_s) and increased shunt resistance (R_{sh}) (Table 1). The device with DIO/NMP has a PCE of 8.14%. Addition of 0.2 wt % SGO also increases the PCE to 8.68%, but this value is lower than that of the 0.2 wt % MGO device. LGO devices show a PCE of 8.22%, which is lower than the efficiency from MGO devices. Addition of 0.2 wt % MGO to P3HT:PC₇₁BM devices provides a device efficiency of 4.34%, which shows an increase compared to the device efficiency of 3.92% from the device without GO NSs (Figure S9 and Table S3). EQE results (Figure 6 and Figure S7–9) show that the conversion of absorbed light to photocurrent is facilitated by the presence of the SGO and MGO NSs unless the GO content is above 0.4 wt % (J – V curves of SGO devices are not shown). The light absorption efficiencies do not vary significantly from sample to sample of GO NSs (Figure 6a). We conclude that the internal quantum efficiencies (IQEs) are increased by the addition of GO NSs over the entire absorption range (Figure 6b).^{64,65} The PL quenching efficiencies of the blend films with and without GO NSs are 99.2% for both films, in comparison to those of their pristine polymers (Figure S10).⁶⁶ Therefore, the J_{sc} and FF increase with the addition of GO NSs is ascribed to the facilitated charge transport rather than to exciton dissociation, as confirmed by increasing μ_h and μ_e from SCLC (Figure 3) and FET devices (Figure 4). However, for concentrations of GO NSs above 0.4 wt %, the overall PCE decreases due to reduced photocurrent generation (Figure S8 and Table S2). When GO is present in large amounts, GO aggregates form, which reduces the photocurrent generation and FF . The presence of LGO significantly reduces the SCLC mobility (Figure 3), because micrometer-sized GO NSs impede the vertical carrier transport in the BHJ photoactive layer due to the lateral GO geometry. Thus, the increase in photovoltaic efficiency requires the addition of appropriately sized GO NSs at proper concentrations.

3.4. Recombination Dynamics of OPV Devices with Size-Selected GO NSs. To determine the effects of the GO NS sizes on recombination dynamics, we evaluated the charge

Table 1. Summary of the Photovoltaic Parameters in PTB7:PC₇₁BM Inverted Devices Prepared with Various-Sized GO NSs (0.2 wt %)^a

devices	V_{oc} [V]	J_{sc} [mA cm ⁻²]	FF [%]	PCE [%]	R_s [Ω cm ²]	R_{sh} [Ω cm ²]
without GO NSs						
with DIO	0.74 ± 0.01	17.2 ± 0.3	62.4 ± 0.2	7.94 ± 0.32	2.52 ± 0.31	1205 ± 21
with NMP	0.74 ± 0.01	17.4 ± 0.3	63.2 ± 0.2	8.14 ± 0.24	2.42 ± 0.25	1225 ± 32
with GO NSs						
SGO	0.74 ± 0.01	17.5 ± 0.2	67.1 ± 0.3	8.68 ± 0.41	2.25 ± 0.15	1352 ± 40
MGO	0.74 ± 0.01	18.0 ± 0.1	69.1 ± 0.3	9.09 ± 0.12	1.91 ± 0.17	1425 ± 38
LGO	0.74 ± 0.01	17.3 ± 0.2	64.2 ± 0.2	8.22 ± 0.28	2.47 ± 0.21	1250 ± 20

^aThose were compared to the values of devices without GO NSs.

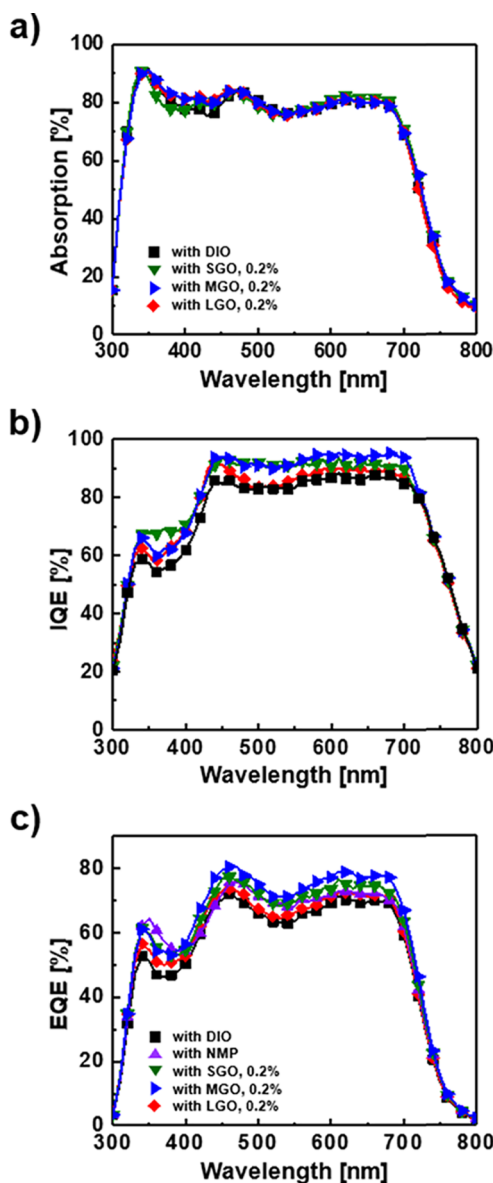


Figure 6. (a) Absorption efficiencies, (b) internal quantum efficiencies, and (c) external quantum efficiencies of inverted devices prepared with active layers having GO NSs of various sizes compared to the values of devices without GO NSs (with DIO and with NMP).

carrier lifetimes ($\tau_{\Delta n}$) and recombination reaction orders (R) by measuring TPV/TPC (Figure 7a).^{54–56} The TPV measurement was performed in order to evaluate $\tau_{\Delta n}$ for OPV devices under open-circuit conditions and various illuminations in which a weak and pulsed optical perturbation is applied (Figure 7a). To determine the number of carrier density (n), TPC was measured in conjunction with TPV under short-circuit conditions with the same perturbation and range of illumination intensities as in the TPV measurements (Figure 7a). $\tau_{\Delta n}$ under 1 sun illumination increases from 5.16×10^{-5} to 7.60×10^{-5} s by adding 0.2 wt % SGO and to 7.75×10^{-5} s by adding 0.2 wt % MGO but decreases to 5.13×10^{-5} s by adding LGO. n also increases from 2.71×10^{16} to 2.92×10^{16} cm^{-3} by adding SGO and to 2.96×10^{16} cm^{-3} by adding MGO but decreases to 2.66×10^{16} cm^{-3} by adding LGO. Figure 7b shows $\tau_{\Delta n}$ versus n for devices with SGO, MGO, and LGO NSs and without any GO NSs. From this, the

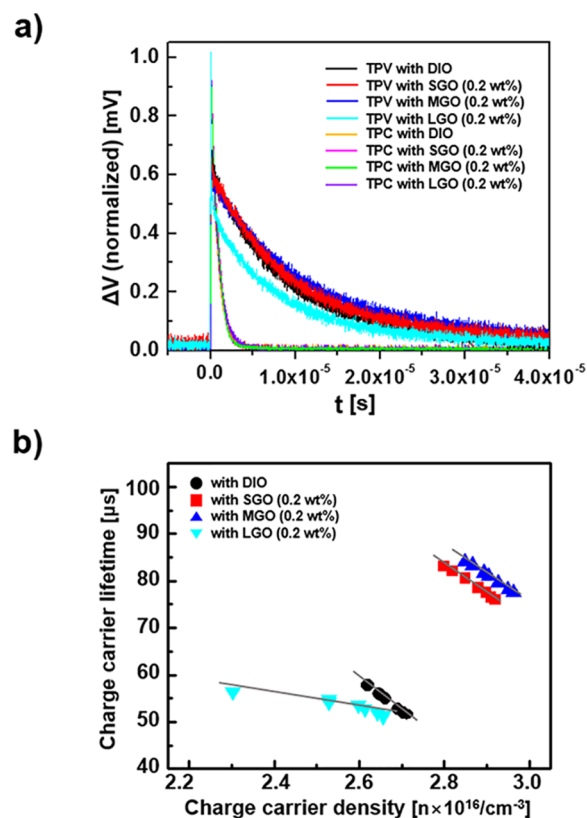


Figure 7. (a) TPV/TPC transitions acquired for PTB7:PC₇₁BM devices. (b) Charge carrier lifetime as a function of the charge carrier density of PTB7:PC₇₁BM devices with SGO, MGO, and LGO and without GO NSs (with DIO).

recombination exponent (λ) and R were estimated as described in the Experimental Section (eq 3). R is reduced by the addition of GO NSs, from 4.32 for the DIO device to 3.14, 3.09, and 2.56 for the SGO, MGO, and LGO devices, respectively. The use of SGO and MGO in OPV devices increases their $\tau_{\Delta n}$ and n and decreases their R compared to the device without GO; these changes indicate that addition of GO NSs significantly reduces non-geminate recombination, possibly as a result of facilitated carrier transport. Also, these results of the reduced non-geminate recombination are in agreement with the trends in the J_{sc} and FF values from SGO and MGO devices (Figure 5 and Table 1). In the presence of LGO, $\tau_{\Delta n}$ and n and resulting device efficiencies are lower than in the SGO and MGO devices. All devices have R higher than two, which indicates that besides non-geminate recombination, some other causes such as energetic traps and morphological traps may also be present.

In this study, we have tuned the multifunctional properties of GO NSs and added those to the photoactive layer, which influence the complex morphology and optoelectronic properties. This approach requires the use of size-selected GO NSs, with NMP as an appropriate solvent. As a result, the non-geminate recombination of charges is reduced, and photovoltaic efficiencies are improved by an increase in charge extraction to the electrodes. This effective strategy of using size-selected GO NSs in OPVs will provide a new method to further improve the OPV efficiency.

4. CONCLUSIONS

We fabricated SGO, MGO, and LGO NSs, which have different size distributions in ranges from several hundreds of nanometers to several micrometers. These GO NS samples were incorporated in PTB7:PC₇₁BM photoactive layers. The LGO provides a large aromatic region with sp²-hybridization, which causes an increased electron delocalization; LGO also has decreased edges with carboxylic functional groups, which decreases the repulsion between GO NSs. The reduced repulsive interaction decreases the dispersion stability of LGO, so the LGO and BHJ active layer developed an aggregated morphology. The electron delocalization with an increase in GO size increases p-doping and achieves high carrier mobilities in SCLC and FET devices. The SCLC mobility is highest in the MGO device with a size distribution of hundreds of nanometers, and charge transport is facilitated by increasing carrier mobilities. The increased carrier transport in MGO devices decreases the non-geminate recombination; the carrier lifetime under 1 sun illumination increases from 5.16×10^{-5} to 7.75×10^{-5} s, and the reaction order of non-geminate recombination is reduced from 4.32 to 3.09. Consequently, the MGO sample provides the PCE of 9.21%, FF of 69.4%, PCE of 8.27%, and FF of 70.5% in inverted and normal PTB7:PC₇₁BM devices, respectively. The PCE of the MGO device is ~16 and ~23% higher than the value of the device without GO NSs in inverted and normal devices, respectively. Therefore, the physical process of sonication is an effective strategy to control GO sizes and, the incorporation of size-selected GO NSs into photoactive layers can significantly improve the efficiencies of OPV devices.

■ ASSOCIATED CONTENT

Supporting Information

The Supporting Information is available free of charge on the ACS Publications website at DOI: 10.1021/acsami.8b22073.

Summary of photovoltaic properties; XPS, FT-IR, C₁₃-NMR, and Raman spectra of GO nanosheets; SEM images of GO nanosheets; AFM images and 2D-GIXRD patterns of blend morphologies; *J*-*V* and EQE results of the devices; and PL spectra of the pristine and blend films (PDF)

■ AUTHOR INFORMATION

Corresponding Authors

*E-mail: jthan@keri.re.kr (J.T.H.).

*E-mail: kwcho@postech.ac.kr (K.C.).

ORCID

Joong Tark Han: 0000-0002-3351-3975

Kilwon Cho: 0000-0003-0321-3629

Notes

The authors declare no competing financial interest.

■ ACKNOWLEDGMENTS

This research was supported by a grant (code no. 2011-0031628 and 2014M3A6A5060953) from the Center for Advanced Soft Electronics under the Global Frontier Research Program of the Ministry of Science and ICT, Korea. This work was supported by the National Research Foundation of Korea (NRF) and the Center for Women In Science, Engineering and Technology (WISSET) grant funded by the Ministry of Science and ICT (MSIT) under the Program for Returners

into R&D. GIXRD patterns of blend films were obtained at the 3C and 9A beamlines at the Pohang Accelerator Laboratory (PAL), Korea.

■ REFERENCES

- (1) Yu, G.; Gao, J.; Hummelen, J. C.; Wudl, F.; Heeger, A. J. Polymer Photovoltaic Cells: Enhanced Efficiencies Via a Network of Internal Donor-Acceptor Heterojunctions. *Science* **1995**, *270*, 1789–1791.
- (2) Zhao, J.; Li, Y.; Yang, G.; Jiang, K.; Lin, H.; Ade, H.; Ma, W.; Yan, H. Efficient Organic Solar Cells Processed from Hydrocarbon Solvents. *Nat. Energy* **2016**, *1*, 15027.
- (3) Liu, Y.; Zhao, J.; Li, Z.; Mu, C.; Ma, W.; Hu, H.; Jiang, K.; Lin, H.; Ade, H.; Yan, H. Aggregation and Morphology Control Enables Multiple Cases of High-Efficiency Polymer Solar Cells. *Nat. Commun.* **2014**, *5*, 5293.
- (4) Lee, J.; Sin, D. H.; Moon, B.; Shin, J.; Kim, H. G.; Kim, M.; Cho, K. Highly Crystalline Low-Bandgap Polymer Nanowires towards High-Performance Thick-Film Organic Solar Cells Exceeding 10% Power Conversion Efficiency. *Energy Environ. Sci.* **2017**, *10*, 247–257.
- (5) Li, S.; Ye, L.; Zhao, W.; Zhang, S.; Mukherjee, S.; Ade, H.; Hou, J. Energy-Level Modulation of Small-Molecule Electron Acceptors to Achieve over 12% Efficiency in Polymer Solar Cells. *Adv. Mater.* **2016**, *28*, 9423–9429.
- (6) Zheng, Z.; Awartani, O. M.; Gautam, B.; Liu, D.; Qin, Y.; Li, W.; Bataller, A.; Gundogdu, K.; Ade, H.; Hou, J. Efficient Charge Transfer and Fine-Tuned Energy Level Alignment in a THF-Processed Fullerene-Free Organic Solar Cell with 11.3% Efficiency. *Adv. Mater.* **2017**, *29*, 1604241.
- (7) Zhao, W.; Li, S.; Yao, H.; Zhang, S.; Zhang, Y.; Yang, B.; Hou, J. Molecular Optimization Enables over 13% Efficiency in Organic Solar Cells. *J. Am. Chem. Soc.* **2017**, *139*, 7148–7151.
- (8) Cui, Y.; Yao, H.; Gao, B.; Qin, Y.; Zhang, S.; Yang, B.; He, C.; Xu, B.; Hou, J. Fine-Tuned Photoactive and Interconnection Layers for Achieving over 13% Efficiency in a Fullerene-Free Tandem Organic Solar Cell. *J. Am. Chem. Soc.* **2017**, *139*, 7302–7309.
- (9) Fei, Z.; Eisner, F. D.; Jiao, X.; Azzouzi, M.; Rohr, J. A.; Han, Y.; Shahid, M.; Chesman, A. S. R.; Easton, C. D.; McNeil, C. R.; Anthopoulos, T. D.; Nelson, J.; Heeney, M. An Alkylated Indacenodithieno[3,2-*b*]thiophene-Based Nonfullerene Acceptor with High Crystallinity Exhibiting Single Junction Solar Cell Efficiencies Greater than 13% with Low Voltage Losses. *Adv. Mater.* **2018**, *30*, 1705209.
- (10) Baran, D.; Kirchartz, T.; Wheeler, S.; Dimitrov, S.; Abdelsamir, M.; Gorman, J.; Ashraf, R. S.; Holliday, S.; Wadsworth, A.; Gasparini, N.; Kaienburg, P.; Yan, H.; Amassian, A.; Brabec, C. J.; Durrant, J. R.; McCulloch, I. Reduced Voltage Losses Yield 10% Efficient Fullerene Free Organic Solar Cells with >1 V Open Circuit Voltages. *Energy Environ. Sci.* **2016**, *9*, 3783–3793.
- (11) Li, W.; Ye, L.; Li, S.; Yao, H.; Ade, H.; Hou, J. A High-Efficiency Organic Solar Cell Enabled by the Strong Intramolecular Electron Push–Pull Effect of the Nonfullerene Acceptor. *Adv. Mater.* **2018**, *30*, 1707170.
- (12) Li, S.; Ye, L.; Zhao, W.; Yan, H.; Yang, B.; Liu, D.; Li, W.; Ade, H.; Hou, J. A Wide Band Gap Polymer with a Deep Highest Occupied Molecular Orbital Level Enables 14.2% Efficiency in Polymer Solar Cells. *J. Am. Chem. Soc.* **2018**, *140*, 7159–7167.
- (13) Brabec, C. J.; Heeney, M.; McCulloch, I.; Nelson, J. Influence of Blend Microstructure on Bulk Heterojunction Organic Photovoltaic Performance. *Chem. Soc. Rev.* **2011**, *40*, 1185–1199.
- (14) Liu, F.; Gu, Y.; Shen, X.; Ferdous, S.; Wang, H.-W.; Russell, T. P. Characterization of the Morphology of Solution-Processed Bulk Heterojunction Organic Photovoltaics. *Prog. Polym. Sci.* **2013**, *38*, 1990–2052.
- (15) Huang, Y.; Kramer, E. J.; Heeger, A. J.; Bazan, G. C. Bulk Heterojunction Solar Cells: Morphology and Performance Relationships. *Chem. Rev.* **2014**, *114*, 7006–7043.

- (16) Salleo, A.; Kline, R. J.; DeLongchamp, D. M.; Chabynyc, M. L. Microstructural Characterization and Charge Transport in Thin Films of Conjugated Polymers. *Adv. Mater.* **2010**, *22*, 3812–3838.
- (17) Lee, H.; Park, C.; Sin, D. H.; Park, J. H.; Cho, K. Recent Advances in Morphology Optimization for Organic Photovoltaics. *Adv. Mater.* **2018**, 1800453.
- (18) Liao, H.-C.; Ho, C.-C.; Chang, C.-Y.; Jao, M.-H.; Darling, S. B.; Su, W.-F. Additives for Morphology Control in High-Efficiency Organic Solar Cells. *Mater. Today* **2013**, *16*, 326–336.
- (19) Vohra, V.; Higashimine, K.; Murakami, T.; Murata, H. Addition of Regiorandom Poly(3-Hexylthiophene) to Solution Processed Poly(3-Hexylthiophene):[6,6]-Phenyl-C61-Butyric Acid Methyl Ester Graded Bilayers to Tune the Vertical Concentration Gradient. *Appl. Phys. Lett.* **2012**, *101*, 173301.
- (20) Kim, M.; Lee, J.; Jo, S. B.; Sin, D. H.; Ko, H.; Lee, H.; Lee, S. G.; Cho, K. Critical Factors Governing Vertical Phase Separation in Polymer-PCBM Blend Films for Organic Solar Cells. *J. Mater. Chem. A* **2016**, *4*, 15522–15535.
- (21) Kim, M.; Kim, J.-H.; Choi, H. H.; Park, J. H.; Jo, S. B.; Sim, M.; Kim, J. S.; Jinnai, H.; Park, Y. D.; Cho, K. Electrical Performance of Organic Solar Cells with Additive-Assisted Vertical Phase Separation in the Photoactive Layer. *Adv. Energy Mater.* **2014**, *4*, 1300612.
- (22) Kim, J.-H.; Gadisa, A.; Schaefer, C.; Yao, H.; Gautam, B. R.; Balar, N.; Ghasemi, M.; Constantinou, I.; So, F.; O'Connor, B. T.; Gundogdu, K.; Hou, J.; Ade, H. Strong Polymer Molecular Weight-Dependent Material Interactions: Impact on the Formation of the Polymer/Fullerene Bulk Heterojunction Morphology. *J. Mater. Chem. A* **2017**, *5*, 13176–13188.
- (23) Kim, J.-H.; Kim, M.; Jinnai, H.; Shin, T. J.; Kim, H.; Park, J. H.; Jo, S. B.; Cho, K. Organic Solar Cells Based on Three-Dimensionally Percolated Polythiophene Nanowires with Enhanced Charge Transport. *ACS Appl. Mater. Interfaces* **2014**, *6*, 5640–5650.
- (24) Zhao, W.; Li, S.; Zhang, S.; Liu, X.; Hou, J. Ternary Polymer Solar Cells based on Two Acceptors and One Donor for Achieving 12.2% Efficiency. *Adv. Mater.* **2017**, *29*, 1604059.
- (25) Baran, D.; Ashraf, R. S.; Hanifi, D. A.; Abdelsamie, M.; Gasparini, N.; Röhr, J. A.; Holliday, S.; Wadsworth, A.; Lockett, S.; Neophytou, M.; Emmott, C. M. J.; Nelson, J.; Brabec, C. J.; Amassian, A.; Salleo, A.; Kirchartz, T.; Durrant, J. R.; McCulloch, I. Reducing the Efficiency-Stability-Cost Gap of Organic Photovoltaics with Highly Efficient and Stable Small Molecule Acceptor Ternary Solar Cells. *Nat. Mater.* **2017**, *16*, 363–370.
- (26) Kim, J.-H.; Schaefer, C.; Ma, T.; Zhao, J.; Turner, J.; Ghasemi, M.; Constantinou, I.; So, F.; Yan, H.; Gadisa, A.; Ade, H. The Critical Impact of Material and Process Compatibility on the Active Layer Morphology and Performance of Organic Ternary Solar Cells. *Adv. Energy Mater.* **2018**, 1802293.
- (27) Gasparini, N.; Jiao, X.; Heumueller, T.; Baran, D.; Matt, G. J.; Fladischer, S.; Spiecker, E.; Ade, H.; Brabec, C. J.; Ameri, T. Designing Ternary Blend Bulk Heterojunction Solar Cells with Reduced Carrier Recombination and a Fill Factor of 77%. *Nat. Energy* **2016**, *1*, 16118.
- (28) Wang, D. H.; Kim, D. Y.; Choi, K. W.; Seo, J. H.; Im, S. H.; Park, J. H.; Park, O. O.; Heeger, A. J. Enhancement of Donor-Acceptor Polymer Bulk Heterojunction Solar Cell Power Conversion Efficiencies by Addition of Au Nanoparticles. *Angew. Chem., Int. Ed.* **2011**, *50*, 5519–5523.
- (29) Kim, C.-H.; Cha, S.-H.; Kim, S. C.; Song, M.; Lee, J.; Shin, W. S.; Moon, S.-J.; Bahng, J. H.; Kotov, N. A.; Jin, S.-H. Silver Nanowire Embedded in P3HT: PCBM for High-Efficiency Hybrid Photovoltaic Device Applications. *ACS Nano* **2011**, *5*, 3319–3325.
- (30) Atwater, H. A.; Polman, A. Plasmonics for Improved Photovoltaic Devices. *Nat. Mater.* **2010**, *9*, 205–213.
- (31) Choi, H.; Ko, S.-J.; Choi, Y.; Joo, P.; Kim, T.; Lee, B. R.; Jung, J.-W.; Choi, H. J.; Cha, M.; Jeong, J.-R.; Hwang, I.-W.; Song, M. H.; Kim, B.-S.; Kim, J. Y. Versatile Surface Plasmon Resonance of Carbon-Dot-Supported Silver Nanoparticles in Polymer Optoelectronic Devices. *Nat. Photonics* **2013**, *7*, 732–738.
- (32) Wu, J.-L.; Chen, F.-C.; Hsiao, Y.-S.; Chien, F.-C.; Chen, P.; Kuo, C.-H.; Huang, M. H.; Hsu, C.-S. Surface Plasmonic Effects of Metallic Nanoparticles on the Performance of Polymer Bulk Heterojunction Solar Cells. *ACS Nano* **2011**, *5*, 959–967.
- (33) Lee, J. H.; Park, J. H.; Kim, J. S.; Lee, D. Y.; Cho, K. High Efficiency Polymer Solar Cells with Wet Deposited Plasmonic Gold Nanodots. *Org. Electron.* **2009**, *10*, 416–420.
- (34) Lee, C.-K.; Pao, C.-W.; Chen, C.-W. Correlation of Nanoscale Organizations of Polymer and Nanocrystals in Polymer/Inorganic Nanocrystal Bulk Heterojunction Hybrid Solar Cells: Insights from Multiscale Molecular Simulations. *Energy Environ. Sci.* **2013**, *6*, 307–315.
- (35) Ning, Z.; Voznyy, O.; Pan, J.; Hoogland, S.; Adinolfi, V.; Xu, J.; Li, M.; Kirmani, A. R.; Sun, J.-P.; Minor, J.; Kemp, K. W.; Dong, H.; Rollny, L.; Labelle, A.; Carey, G.; Sutherland, B.; Hill, I.; Amassian, A.; Liu, H.; Tang, J.; Bakr, O. M.; Sargent, E. H. Air-Stable n-Type Colloidal Quantum Dot Solids. *Nat. Mater.* **2014**, *13*, 822–828.
- (36) Bonaccorso, F.; Balis, N.; Stylianakis, M. M.; Savarese, M.; Adamo, C.; Gemmi, M.; Pellegrini, V.; Stratakis, E.; Kymakis, E. Functionalized Graphene as an Electron-Cascade Acceptor for Air-Processed Organic Ternary Solar Cells. *Adv. Funct. Mater.* **2015**, *25*, 3870–3880.
- (37) Lee, J. M.; Park, J. S.; Lee, S. H.; Kim, H.; Yoo, S.; Kim, S. O. Selective Electron- or Hole-Transport Enhancement in Bulk-Heterojunction Organic Solar Cells with N- or B-Doped Carbon Nanotubes. *Adv. Mater.* **2011**, *23*, 629–633.
- (38) Liu, J.; Xue, Y.; Gao, Y.; Yu, D.; Durstock, M.; Dai, L. Hole and Electron Extraction Layers Based on Graphene Oxide Derivatives for High-Performance Bulk Heterojunction Solar Cells. *Adv. Mater.* **2012**, *24*, 2228–2233.
- (39) Baek, S.-W.; Kim, J. H.; Kang, J.; Lee, H.; Park, J. Y.; Lee, J.-Y. Enhancing the Internal Quantum Efficiency and Stability of Organic Solar Cells via Metallic Nanofunnels. *Adv. Energy Mater.* **2015**, *5*, 1501393.
- (40) Lu, L.; Xu, T.; Chen, W.; Lee, J. M.; Luo, Z.; Jung, I. H.; Park, H. I.; Kim, S. O.; Yu, L. The Role of N-Doped Multiwall Carbon Nanotubes in Achieving Highly Efficient Polymer Bulk Heterojunction Solar Cells. *Nano Lett.* **2013**, *13*, 2365–2369.
- (41) Jeong, S. Y.; Kim, S. H.; Han, J. T.; Jeong, H. J.; Jeong, S. Y.; Lee, G.-W. Highly Concentrated and Conductive Reduced Graphene Oxide Nanosheets by Monovalent Cation- π Interaction: Toward Printed Electronics. *Adv. Funct. Mater.* **2012**, *22*, 3307–3314.
- (42) Kim, H.; Kim, H. H.; Jang, J. I.; Lee, S. K.; Lee, G.-W.; Han, J. T.; Cho, K. Doping Graphene with an Atomically Thin Two Dimensional Molecular Layer. *Adv. Mater.* **2014**, *26*, 8141–8146.
- (43) Lee, B. R.; Kim, J.-W.; Kang, D.; Lee, D. W.; Ko, S.-J.; Lee, H. J.; Lee, C.-L.; Kim, J. Y.; Shin, H. S.; Song, M. H. Highly Efficient Polymer Light-Emitting Diodes Using Graphene Oxide as a Hole Transport Layer. *ACS Nano* **2012**, *6*, 2984–2991.
- (44) Li, S.-S.; Tu, K.-H.; Lin, C.-C.; Chen, C.-W.; Chhowalla, M. Solution-Processable Graphene Oxide as an Efficient Hole Transport Layer in Polymer Solar Cells. *ACS Nano* **2010**, *4*, 3169–3174.
- (45) Han, J. T.; Kim, J. S.; Jo, S. B.; Kim, S. H.; Kim, J. S.; Kang, B.; Jeong, H. J.; Jeong, S. Y.; Lee, G.-W.; Cho, K. Graphene Oxide as a Multi-Functional p-Dopant of Transparent Single-Walled Carbon Nanotube Films for Optoelectronic Devices. *Nanoscale* **2012**, *4*, 7735–7742.
- (46) Yu, J. C.; Jang, J. I.; Lee, B. R.; Lee, G.-W.; Han, J. T.; Song, M. H. Highly Efficient Polymer-Based Optoelectronic Devices Using PEDOT:PSS and a GO Composite Layer as a Hole Transport Layer. *ACS Appl. Mater. Interfaces* **2014**, *6*, 2067–2073.
- (47) Kim, H. H.; Yang, J. W.; Jo, S. B.; Kang, B.; Lee, S. K.; Bong, H.; Lee, G.; Kim, K. S.; Cho, K. Substrate-Induced Solvent Intercalation for Stable Graphene Doping. *ACS Nano* **2013**, *7*, 1155–1162.
- (48) Gao, Y.; Yip, H.-L.; Chen, K.-S.; O'Malley, K. M.; Acton, O.; Sun, Y.; Ting, G.; Chen, H.; Jen, A. K.-Y. Surface Doping of Conjugated Polymers by Graphene Oxide and Its Application for Organic Electronic Devices. *Adv. Mater.* **2011**, *23*, 1903–1908.

- (49) Jun, G. H.; Jin, S. H.; Lee, B.; Kim, B. H.; Chae, W.-S.; Hong, S. H.; Jeon, S. Enhanced Conduction and Charge-Selectivity by N-Doped Graphene Flakes in the Active Layer of Bulk-Heterojunction Organic Solar Cells. *Energy Environ. Sci.* **2013**, *6*, 3000–3006.
- (50) Kim, J. K.; Park, M. J.; Kim, S. J.; Wang, D. H.; Cho, S. P.; Bae, S.; Park, J. H.; Hong, B. H. Balancing Light Absorptivity and Carrier Conductivity of Graphene Quantum Dots for High-Efficiency Bulk Heterojunction Solar Cells. *ACS Nano* **2013**, *7*, 7207–7212.
- (51) Erickson, K.; Erni, R.; Lee, Z.; Alem, N.; Gannett, W.; Zettl, A. Determination of the Local Chemical Structure of Graphene Oxide and Reduced Graphene Oxide. *Adv. Mater.* **2010**, *22*, 4467–4472.
- (52) Wang, X.; Bai, H.; Shi, G. Size Fractionation of Graphene Oxide Sheets by pH-Assisted Selective Sedimentation. *J. Am. Chem. Soc.* **2011**, *133*, 6338–6342.
- (53) Lin, X.; Shen, X.; Zheng, Q.; Yousefi, N.; Ye, L.; Mai, Y.-W.; Kim, J.-K. Fabrication of Highly-Aligned, Conductive, and Strong Graphene Papers Using Ultralarge Graphene Oxide Sheets. *ACS Nano* **2012**, *6*, 10708–10719.
- (54) Credgington, D.; Jamieson, F. C.; Walker, B.; Nguyen, T.-Q.; Durrant, J. R. Quantification of Geminate and Non-Geminate Recombination Losses within a Solution-Processed Small-Molecule Bulk Heterojunction Solar Cell. *Adv. Mater.* **2012**, *24*, 2135–2141.
- (55) Ameri, T.; Heumüller, T.; Min, J.; Li, N.; Matt, G.; Scherf, U.; Brabec, C. J. IR Sensitization of an Indene-C60 Bisadduct (ICBA) in Ternary Organic Solar Cells. *Energy Environ. Sci.* **2013**, *6*, 1796–1801.
- (56) Maurano, A.; Shuttle, C. G.; Hamilton, R.; Ballantyne, A. M.; Nelson, J.; Zhang, W.; Heeney, M.; Durrant, J. R. Transient Optoelectronic Analysis of Charge Carrier Losses in a Selenophene/Fullerene Blend Solar Cell. *J. Phys. Chem. C* **2011**, *115*, 5947–5957.
- (57) Hummers, W. S., Jr.; Offeman, R. E. Preparation of Graphitic Oxide. *J. Am. Chem. Soc.* **1958**, *80*, 1339–1339.
- (58) Goodman, A. M.; Rose, A. Double Extraction of Uniformly Generated Electron-Hole Pairs from Insulators with Noninjecting Contacts. *J. Appl. Phys.* **1971**, *42*, 2823–2830.
- (59) Mihailetchi, V. D.; Xie, H. X.; de Boer, B.; Koster, L. J. A.; Blom, P. W. M. Charge Transport and Photocurrent Generation in Poly (3-Hexylthiophene): Methanofullerene Bulk-Heterojunction Solar Cells. *Adv. Funct. Mater.* **2006**, *16*, 699–708.
- (60) Mattevi, C.; Eda, G.; Agnoli, S.; Miller, S.; Mkhoyan, K. A.; Celik, O.; Mastrogianni, D.; Granozzi, G.; Garfunkel, E.; Chhowalla, M. Evolution of Electrical, Chemical, and Structural Properties of Transparent and Conducting Chemically Derived Graphene Thin Films. *Adv. Funct. Mater.* **2009**, *19*, 2577–2583.
- (61) Liang, Y.; Xu, Z.; Xia, J.; Tsai, S.-T.; Wu, Y.; Li, G.; Ray, C.; Yu, L. For the Bright Future-Bulk Heterojunction Polymer Solar Cells with Power Conversion Efficiency of 7.4%. *Adv. Mater.* **2010**, *22*, E135–E138.
- (62) Rivnay, J.; Mannsfeld, S. C. B.; Miller, C. E.; Salleo, A.; Toney, M. F. Quantitative Determination of Organic Semiconductor Microstructure from the Molecular to Device Scale. *Chem. Rev.* **2012**, *112*, 5488–5519.
- (63) Zhang, L.; Colella, N. S.; Liu, F.; Trahan, S.; Baral, J. K.; Winter, H. H.; Mannsfeld, S. C. B.; Briseno, A. L. Synthesis, Electronic Structure, Molecular Packing/Morphology Evolution, and Carrier Mobilities of Pure Oligo-/Poly(alkylthiophenes). *J. Am. Chem. Soc.* **2013**, *135*, 844–854.
- (64) Park, S. H.; Roy, A.; Beaupré, S.; Cho, S.; Coates, N.; Moon, J. S.; Moses, D.; Leclerc, M.; Lee, K.; Heeger, A. J. Bulk Heterojunction Solar Cells with Internal Quantum Efficiency Approaching 100%. *Nat. Photonics* **2009**, *3*, 297–302.
- (65) Jo, J.; Na, S.-I.; Kim, S.-S.; Lee, T.-W.; Chung, Y.; Kang, S.-J.; Vak, D.; Kim, D.-Y. Three-Dimensional Bulk Heterojunction Morphology for Achieving High Internal Quantum Efficiency in Polymer Solar Cells. *Adv. Funct. Mater.* **2009**, *19*, 2398–2406.
- (66) Baran, D.; Li, N.; Breton, A.-C.; Osvet, A.; Ameri, T.; Leclerc, M.; Brabec, C. J. Qualitative Analysis of Bulk-Heterojunction Solar Cells without Device Fabrication: An Elegant and Contactless Method. *J. Am. Chem. Soc.* **2014**, *136*, 10949–10955.